Monthly Notices
of the
ROYAL ASTRONOMICAL SOCIETY

MNRAS **432,** 693–701 (2013)
Advance Access publication 2013 April 17

doi:10.1093/mnras/stt505

Warm *Spitzer* occultation photometry of WASP-26b at 3.6 and 4.5 μm

D. P. Mahtani,[1]★ P. F. L. Maxted,[1] D. R. Anderson,[1] A. M. S. Smith,[1]† B. Smalley,[1] J. Tregloan-Reed,[1] J. Southworth,[1] N. Madhusudhan,[2] A. Collier Cameron,[3] M. Gillon,[4] J. Harrington,[5] C. Hellier,[1] D. Pollacco,[6] D. Queloz,[7] A. H. M. J. Triaud[7] and R. G. West[8]

[1]*Astrophysics Group, Keele University, Keele, Staffordshire, ST5 5BG, UK*
[2]*Department of Physics and Department of Astronomy, Yale University, New Haven, CT 06520-8101, USA*
[3]*SUPA, School of Physics and Astronomy, University of St Andrews, North Haugh, Fife KY16 9SS, UK*
[4]*Institut d'Astrophysique et de Géophysique, Université de Liège, Allée du 6 Août, 17, Bat. B5C, B-4000 Liège 1, Belgium*
[5]*Planetary Sciences Group, Department of Physics, University of Central Florida, Orlando, FL 32816-2385, USA*
[6]*Department of Physics, University of Warwick, Gibbet Hill Road, Coventry CV4 7AL, UK*
[7]*Observatoire astronomique de l'Université de Genève 51 ch. des Maillettes, 1290 Sauverny, Switzerland*
[8]*Department of Physics and Astronomy, University of Leicester, Leicester, LE1 7RH, UK*

Accepted 2013 March 19. Received 2013 March 19; in original form 2012 December 20

ABSTRACT

We present new warm *Spitzer* occultation photometry of WASP-26 at 3.6 and 4.5 μm along with new transit photometry taken in the *g, r* and *i* bands. We report the first detection of the occultation of WASP-26b, with occultation depths at 3.6 and 4.5 μm of 0.001 26 ± 0.000 13 and 0.001 49 ± 0.000 16 corresponding to brightness temperatures of 1825 ± 80 and 1725 ± 89 K, respectively. We find that the eccentricity of the orbit is consistent with a circular orbit at the 1σ level ($e = 0.0028^{+0.0097}_{-0.0022}$, 3$\sigma$ upper limit $e < 0.04$). According to the activity–inversion relation of Knutson et al., WASP-26b is predicted to host a thermal inversion. The brightness temperatures deduced from the eclipse depths are consistent with an isothermal atmosphere, although the planet may host a weak thermal inversion given the uncertainties on these values. The data are equally well fitted by atmospheric models with or without a thermal inversion. We find that variation in activity of solar-like stars does not change enough over the time-scales of months or years to change the interpretation of the Knutson et al. activity–inversion relation, provided that the measured activity level is averaged over several nights. Further data are required to fully constrain the thermal structure of the atmosphere because the planet lies very close to the boundary between atmospheres with and without a thermal inversion.

Key words: methods: data analysis – planets and satellites: atmospheres – stars: individual: WASP-26.

1 INTRODUCTION

The first detection of thermal emission from an exoplanet was reported by Deming et al. (2005) and Charbonneau et al. (2005). The teams observed the secondary eclipse of HD 209458 and TrES-1 using the *Spitzer Space Telescope*. Secondary eclipses of many other exoplanets have now been observed (e.g. Machalek et al. 2008; Anderson et al. 2011a; Todorov et al. 2012). Through the spectrophotometry of this event, observed using *Spitzer* and ground-based telescopes, we can build up the spectral energy distribution (SED) of the irradiated hemisphere (day side) of the planet. From the SED we can investigate the atmospheric properties of the day side of the planet. Secondary eclipse observations made with *Spitzer* have shown that some of these exoplanets have temperature inversions (Fortney et al. 2008; Knutson et al. 2009; Madhusudhan & Seager 2010). Thermal inversions are thought to form when gases exist in the upper atmosphere of these exoplanets that are efficient absorbers of optical and ultraviolet light (Fortney et al. 2008). This absorption of radiation causes the temperature of this region of the atmosphere to increase. Gases that have been hypothesized to cause thermal inversions are titanium oxide and vanadium oxide (Spiegel, Silverio & Burrows 2009) and sulphur compounds (Zahnle et al. 2009).

WASP-26b, discovered by Smalley et al. (2010) with SuperWASP (Pollacco et al. 2006), is a one Jupiter mass ($1M_{\rm Jup}$) planet in a 2.8 d orbit around a G0 type star. WASP-26 also has a common

★ E-mail: d.p.mahtani@keele.ac.uk
† Present address: N. Copernicus Astronomical Centre, Polish Academy of Sciences, Bartycka 18, 00-716 Warsaw, Poland.

Table 1. Summary of data used in this analysis.

Observation	Dates	Publication
SuperWASP photometry (400–700 nm filter)	2008 June 30–2008 November 17 2009 June 28–2009 November 17	Smalley et al. (2010)
16 RV spectra from CORALIE (1.2 m Swiss Telescope, La Silla, Chile)	2009 June 19–2009 August 22	Smalley et al. (2010)
30 RV spectra from HARPS (HARPS Spectrograph, ESO 3.6 m telescope, La Silla, Chile)	2010 September 12	Anderson et al. (2011b)
Full transit (Pan-STARRS-*z* filter) (2.0 m Faulkes Telescope South, Siding Spring, Australia)	2009 November 18	Smalley et al. (2010)
Occultation (3.6 μm) (*Spitzer* channel 1)	2010 August 3	This Paper
Occultation (4.5 μm) (*Spitzer* channel 2)	2010 August 7–2010 August 8	This Paper
Full transit (*g, r* and *i* band) (Calar Alto Astronomical Observatory with BUSCA, Almería, Spain)	2010 August 20	This paper

proper motion companion 15 arcsec away (Smalley et al. 2010). Anderson et al. (2011b) conducted an investigation using the Rossiter–McLaughlin (R-M) effect to determine the sky-projected spin–orbit angle of the system. However, their results were inconclusive. Albrecht et al. (2012) constrained the spin–orbit angle of the system to $\lambda = -34^{+36\circ}_{-26}$. In this paper, we present new warm *Spitzer* and ground-based photometry of WASP-26.

2 OBSERVATIONS

We present *Spitzer* (Werner et al. 2004) InfraRed Array Camera (IRAC; Fazio et al. 2004) channel 1 (3.6 μm) and channel 2 (4.5 μm) secondary eclipse (occultation) data taken on 2010 August 3 and 2010 September 7–8, respectively (PI: J Harrington, programme ID 60003). The *Spitzer* data were acquired in full array mode (256 × 256). Also presented are new full transit data taken in the *g, r* and *i* bands (taken simultaneously) using the 2.2 m telescope at the Calar Alto Astronomical Observatory with the Bonn University Simultaneous CAmera (BUSCA) on 2010 August 20. BUSCA is a four channel CCD photometer with 4096 × 4096 pixels per CCD with a plate scale of 0.17 arcsec pixel^{-1}. The BUSCA transit data were obtained using defocused photometry (Southworth et al. 2009a, 2012), and BUSCA was used with a 256 × 1400 pixel window and 2 × 2 binning to reduce the readout time. Table 1 is a summary of the data that we have used in our analysis.

3 DATA REDUCTION

3.1 Transit data reduction

We used an IDL implementation of DAOPHOT (Stetson 1987) to perform synthetic aperture photometry on our BUSCA images, as in Southworth et al. (2009a). Light curves were obtained in the *g, r* and *i* bands. In all three bands, one comparison star was used. We used a target aperture of radius 24 pixels, a sky annulus of inner radius 70 pixels and an outer radius 100 pixels for the *g, r* and *i* bands. The wings of the point spread function (PSF) of the companion star do contaminate the target aperture, but the contribution to the observed flux is negligible. Iterative outlier removal was used on the image values in the sky annulus to remove the effect of the light from the wings of the companion's PSF in the sky annulus. The light curves are shown in Fig. 1.

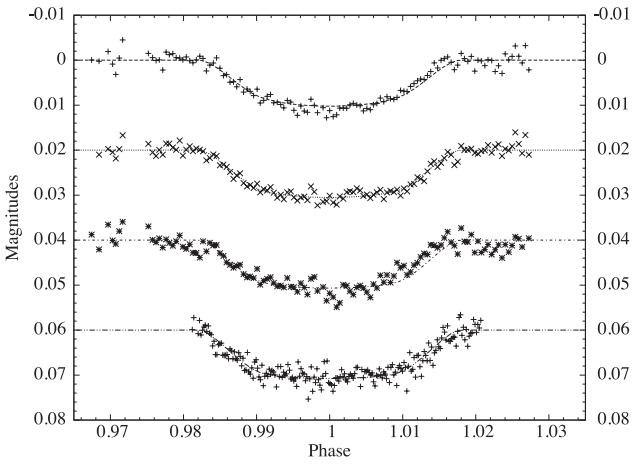

Figure 1. BUSCA and FTS data with best-fitting models (from the top to bottom), *g*-band data, *r*-band data, *i*-band data and the FTS (*z* filter) data.

3.2 *Spitzer* data reduction

The data reduction was conducted using the Image Reduction and Analysis Facility (IRAF)[1] using the same method as Anderson et al. (2011a), described briefly below.

We convert from MJy/sr to electrons using equation (1), where the gain, exposure time and flux conversion factor were taken from the image headers,

$$\text{Factor} = \frac{\text{Gain} \times \text{Exposure Time}}{\text{Flux Conversion Factor}}. \quad (1)$$

Aperture photometry was then conducted using the PHOT procedure in IRAF, using 21 aperture radii in the range 1.5–6 pixels and with a sky annulus of inner radius 8 pixels and outer radius 16 pixels. It was found that the stellar companion to WASP-26 and a bad column in channel 2 data were both inside the sky annulus. However, an iterative 3σ clipping was conducted which excludes those pixels. The error on the photometry was calculated from the photon statistics and the readout noise of the IRAC detectors. The readout noise values were taken from the IDL program SNIRAC_warm.pro;[2] the

[1] IRAF is distributed by the National Optical Astronomy Observatories, which are operated by the Association of Universities for Research in Astronomy, Inc., under cooperative agreement with the National Science Foundation.

Table 2. Proposal parameters of the model used in our MCMC analysis.

T_c	Time of mid-transit
P	Period of planet
ΔF	Depth of transit
T_{14}	Transit duration
b	Impact parameter
K_1	Stellar radial reflex velocity
$T_{\rm eff}$	Effective temperature of the star
[Fe/H]	Metallicity of the star
$\sqrt{e}\cos\omega$, $\sqrt{e}\sin\omega$	e = eccentricity, ω = argument of periastron
$\Delta F_{3.6}$	Depth of secondary eclipse at 3.6 μm
$\Delta F_{4.5}$	Depth of secondary eclipse at 4.5 μm

values for channels 1 and 2 are 9.87 and 9.4 electrons, respectively. The position of the target was measured by fitting a one-dimensional Gaussian to the marginal distributions of flux on x and y image axes. For each data set, the times of mid-exposure were converted to $\mathrm{BJD_{TDB}}$ (Eastman, Siverd & Gaudi 2010) and for the occultation data the light travel time across the system (∼40 s) was accounted for. The light travel time across the system was calculated using the semi-major axis from the output of our initial Markov chain Monte Carlo (MCMC, see below for details of this run) and this time was subtracted from all the *Spitzer* times.

4 ANALYSIS

4.1 MCMC

We explored the parameter space using a Markov chain Monte Carlo (MCMC) algorithm (Collier Cameron et al. 2007; Pollacco et al. 2008; Enoch et al. 2010). The input parameters for the star that were used in the MCMC analysis are $T_{\rm eff} = 5950 \pm 100$ and $[\mathrm{Fe/H}] = -0.02 \pm 0.09$ (Anderson et al. 2011b). Stellar density, which is directly constrained by the transit light curve and the spectroscopic orbit (Seager & Mallén-Ornelas 2003) and the eccentricity of the orbit, is calculated from the proposal parameter values. This is input, together with the latest values of $T_{\rm eff}$ and [Fe/H] (which are controlled by Gaussian priors) into the empirical mass calibration of Enoch et al. (2010) to obtain an estimate of the stellar mass, M_*. At each step in the MCMC procedure, each proposal parameter is perturbed from its previous value by a small, random amount. From the proposal parameters, model light and radial velocity (RV) curves are generated and χ^2 is calculated from their comparison with the data. A step is accepted if χ^2 (our merit function) is lower than for the previous step, and a step with higher χ^2 is accepted with probability $\exp(-\Delta\chi^2)$. In this way, the parameter space around the optimum solution is thoroughly explored. The value and uncertainty for each parameter are taken as the median and central 68.3 per cent confidence interval of the parameter's marginalized posterior probability distribution, respectively (Ford 2006). The median closely approximates the χ^2 minimum for symmetric posteriors such as ours, and is more robust to noise in the case of flat minima. Table 2 show the proposal parameters of the MCMC. We did an initial run which included all the transit photometry, including the SuperWASP photometry, to get a good estimate of the epoch of mid-transit. This value along with its uncertainty was used as a Bayesian prior in subsequent MCMC runs which used all the photometry, including *Spitzer*, but excluding the SuperWASP photometry (to reduce computing time). The transit model used in the analysis was the small-planet approximation of Mandel & Agol (2002) with four-parameter limb darkening coefficients taken from Claret (2004). The limb darkening coefficients were determined using an initial interpolation in $\log g_\star$ and [Fe/H] and an interpolation in $T_{\rm eff}$ at each MCMC step. The limb darkening parameters used for the best-fitting light curves are given in Table 3. For the secondary eclipse, we approximated the star and planet as two uniform discs of constant surface brightness. We fixed the projected spin–orbit angle to the value $\lambda = 0$ in our fit since the HARPS data covering the transit are negligibly affected by the R-M effect. The fit to the optical light curves (Fig. 1) shows that there is some red noise present in the g and i band light curves. We have accounted for the small additional uncertainty due to this noise in our quoted parameter standard errors rather than trying to find an arbitrary model that would improve the fit.

Table 3. Limb darkening coefficients.

Light curve	a_1	a_2	a_3	a_4
FTS	0.655	−0.352	0.645	−0.329
BUSCA (g band)	0.433	0.208	0.496	−0.300
BUSCA (r band)	0.555	0.028	0.445	−0.278
BUSCA (i band)	0.641	−0.267	0.640	−0.338

We checked for any correlations in our proposal parameters and only found the correlation between transit depth, width and impact parameter often seen in ground-based light curves. These correlations are caused by the blurring of the second and third contact points due to limb darkening in the optical light curves. These correlations do not affect our secondary eclipse depth measurements. These correlations are shown in Fig. 2. We also checked that our chain had converged, both by visual inspection and using the Gelmen–Rubin statistic (Gelman et al. 2003; Ford 2006).

4.2 Trend functions and aperture size

Fig. 3 shows an example of the 3.6 μm light curve produced by the photometry in IRAF. There is a steep increase in the measured flux during the first part of the observation. This occurs because the telescope has slewed from its old position to its new position and is adjusting to a new equilibrium. We exclude the data that precedes HJD = 245 5447.37, to remove the major part of the initial ramp. It can be seen that there is a clear periodic trend in the data. This is due to the variation in the position of the target on the detector caused by flexure of the instrument as an electric heater is turned off and on.[3] The IRAC detectors are known to exhibit inhomogeneous intrapixel sensitivity (e.g. Knutson et al. 2008), which means that different parts of the detector are more or less sensitive than others. This, along with the PSF movement, results in the measured flux varying depending on the position of the PSF on the detector. Also, when small apertures are used, pixelation occurs due to the undersampling of the PSF of the target (Anderson et al. 2011a). These systematics will be accounted for in the trend functions as described below. Fig. 4 shows an example of the 4.5 μm data which are less affected by these systematics even though (as it can be seen from Fig. 5) the radial motion of the PSF is greater at 4.5 μm than at 3.6 μm.

[2] http://ssc.spitzer.caltech.edu/warmmission/propkit/som/snirac_warm.pro

[3] http://ssc.spitzer.caltech.edu/warmmission/news/21oct2010memo.pdf

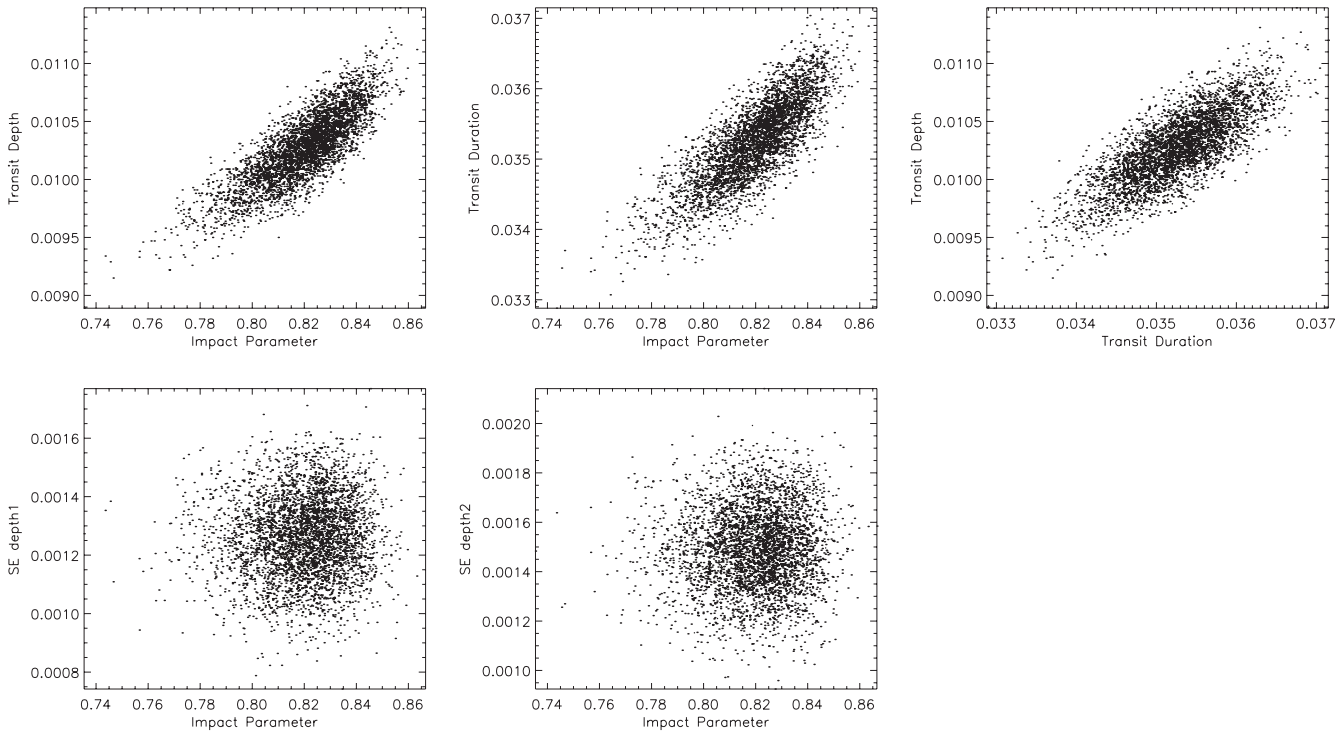

Figure 2. Correlation plots for selected proposal parameters from our MCMC analysis. For clarity we have only plotted a random 2 per cent of the chain values.

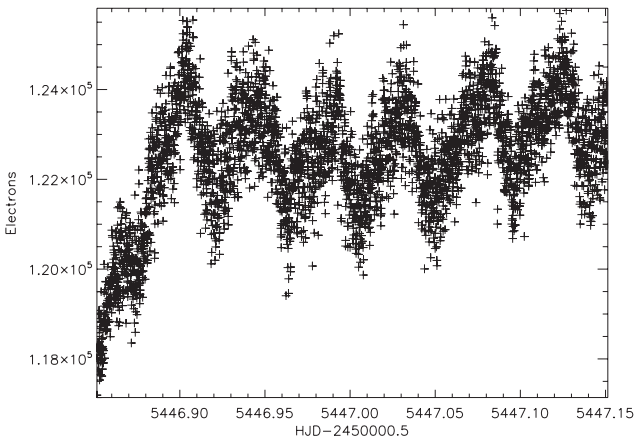

Figure 3. The raw light curve of the 3.6 μm *Spitzer* data extracted using an aperture of 2.4 pixels.

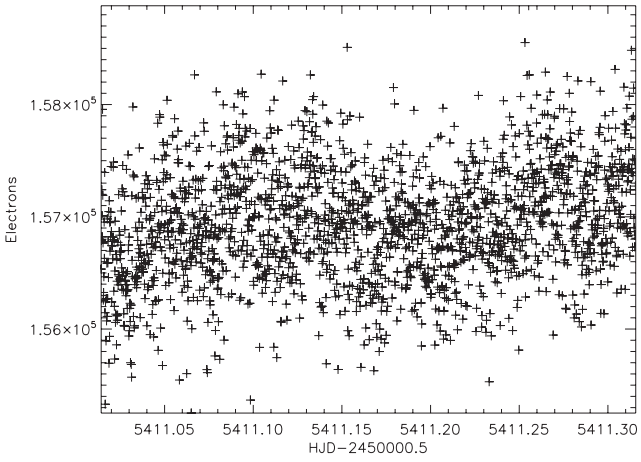

Figure 4. The raw light curve of the 4.5 μm *Spitzer* data extracted using an aperture of 2.4 pixels.

The general form of the trend functions that were used in our analysis is

$$\Delta f = a_0 + a_x \Delta x + a_y \Delta y + a_{xy} \Delta x \Delta y + a_{xx} \Delta x^2 + a_{yy} \Delta y^2 + a_t \Delta t, \quad (2)$$

where $\Delta f = f - \hat{f}$ is the stellar flux relative to its weighted mean, $\Delta x = x - \hat{x}$ and $\Delta y = y - \hat{y}$ are the coordinates of the PSF of the target centre relative to their weighted means, Δt is the time since the beginning of the observation, and a_0, a_x, a_y, a_{xx}, a_{yy} and a_t are coefficients which are free parameters in the MCMC analysis (Anderson et al. 2011a). For each set of trial light-curve model parameters, we calculate the residuals from the model and then calculate the coefficients of the detrending model using singular value decomposition applied to the entire data set. Initially, a linear-in-time and quadratic-in-space trend function was used on all 21 apertures to fit the secondary eclipse data. The rms of the residuals was used to determine the optimal aperture size. Once this was determined, combinations of no trend function, linear and quadratic trend functions in time and space were used on the best aperture to determine the best-fitting trend function.

Initially, this decorrelation was conducted using the positions measured by the one-dimensional Gaussian fit to the target. We also attempted to remove the trends in the data by decorrelating against the radial position (radial distance from the centre of the nearest pixel) instead of the x and y positions independently. The general trend function for the radial decorrelation is

$$\Delta f = b_0 + b_1 r + b_2 r^2 + b_t \Delta t, \quad (3)$$

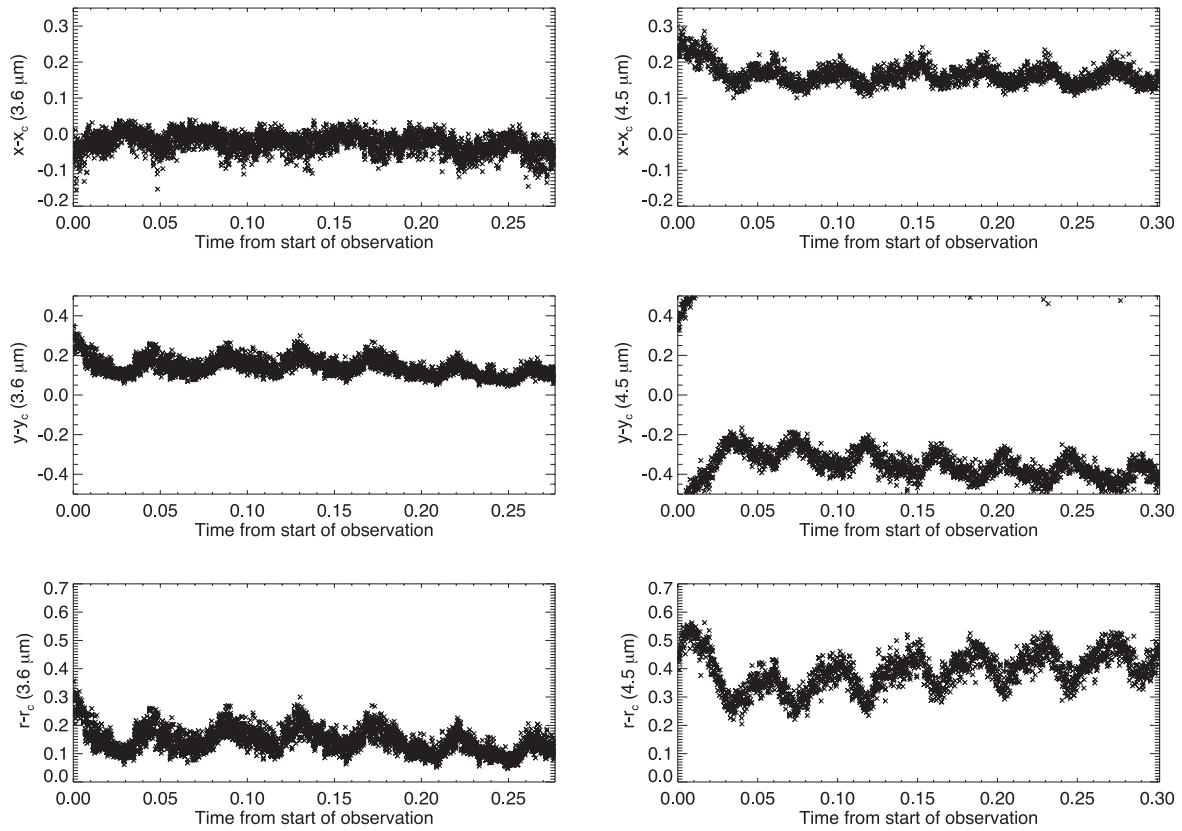

Figure 5. The top, middle and bottom plots of the each column show the distance of the PSF from the nearest pixel centre in x, y and radially in each of the measured wavelengths, respectively.

where b_0, b_1, b_2, b_t are free parameters in the MCMC analysis and r is the radial distance from the centre of the nearest pixel centre. A third method that was attempted was to use target positions in the trend functions measured by fitting a two-dimensional circular Gaussian of fixed full width half-maximum (1.39 pixels in channel 1 and 1.41 pixels in channel 2) to a small region of the images containing the target.

To determine which trend function gave better results, we used the Bayesian information criterion (BIC; Schwarz 1978)

$$\mathrm{BIC} = \chi^2 + k \ln(n), \tag{4}$$

where k is the number of free parameters and n is the number of data points. This method of determining how complicated a model to use only accepts a higher order trend function if the fit improves χ^2 by $\ln(n)$ or better for each additional free parameter.

Using the rms of the residuals it was found that the best aperture to use was 2.4 pixels in both channels. The system parameters are negligibly affected by the choice of aperture radius around this value. It was also found that the rms of the residuals to the channel 1 data was marginally lower when using the position measurements measured by the 2D circular Gaussian method as opposed to 1D Gaussian position measurements (0.002 995 compared to 0.003 054). The channel 2 data gave consistent rms irrespective of the position measurement used. The system parameters were consistent no matter which position measurement system was used. The results shown in Fig. 6 and Table 4 are those using the 2D circular Gaussian method, extracted from the 2.4 pixel aperture and trend functions as described below. We found that the radial decorrelation gave a worse fit to our data compared to that of x and y decorrelation (χ^2 worse by $\sim$3000 at 3.6 μm and $\sim$400 at 4.5 μm).

Using equation (4) it was found that the quadratic-in-space with no time trend function gave the best fit to the data in channel 1 and that the linear-in-space with no time trend function gave the best fit to the data in channel 2. It was found that the addition of the quadratic term for the spatial decorrelation improved our BIC by $\sim$200 in channel 1 and less than $\sim$10 for more complicated models in both channels. We also detrended our data based only on the out-of-eclipse points to see if this affected our measured eclipse depths. It was found that the eclipse depths were consistent with our previous decorrelation.

5 RESULTS AND DISCUSSION

5.1 Eclipse depths and brightness temperatures

We find that the eclipse depths at 3.6 and 4.5 μm are $0.001\,26 \pm 0.000\,13$ and $0.001\,49 \pm 0.000\,16$, respectively. These eclipse depths correspond to brightness temperatures of 1825 ± 80 and 1725 ± 89 K. To find these blackbody temperatures, the expected flux ratios were calculated using Planck functions at different temperatures for the planet and synthetic spectra from stellar models (Kurucz 1991) for the star. These flux ratios were then integrated over the *Spitzer* band passes to calculate the expected measured flux ratio. The temperatures above correspond to the best-fitting Planck function temperature to the individual eclipse depths. The errors were calculated using a simple Monte Carlo method. These temperatures suggest that, on average, the emission at mid-infrared

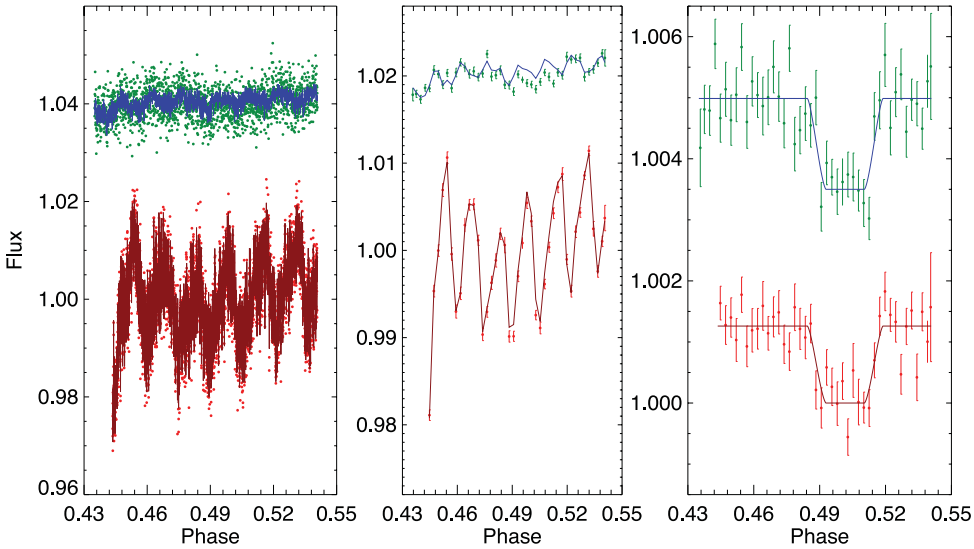

Figure 6. Left: the raw light curves with the trend functions; the upper points denote the channel 2 data and the lower points denote the channel 1 data and the solid lines show the trend functions for each data set. Middle: binned light curves with trend models. Right: the binned light curve with trend function removed and best-fitting eclipse models (solid lines). The secondary eclipse can clearly be seen in both channels.

Table 4. System parameters from our MCMC analysis.

Parameter	Symbol (unit)	Value
Orbital period	P (d)	2.756 611 ±0.000 008
Epoch of mid-transit (BJD, TDB)	T_c	2455 424.108 99 ±0.000 12
Transit duration (from first to fourth contact)	T_{14} (d)	0.097 ±0.002
Duration of transit ingress ≈ duration of transit egress	$T_{12} \approx T_{34}$ (d)	0.024 ±0.002
Planet-to-star area ratio	$\Delta F = R_P^2/R_*^2$	0.0103 ±0.0003
Impact parameter	b	0.82 ±0.02
Orbital inclination	i (°)	82.9 ±0.4
Semi-amplitude of the stellar reflex velocity	K_1 (km s^{-1})	0.138±0.002
Centre-of-mass velocity	γ (km s^{-1})	8.4593 ±0.0001
Argument of periastron	ω (°)	-90^{+200}_{-20}
	$e\cos\omega$	−0.0004 ±0.0007
	$e\sin\omega$	$-0.0011\ ^{+0.0023}_{-0.0110}$
Orbital eccentricity	e	$0.002\,83\ ^{+0.009\,65}_{-0.002\,21}$
Phase of mid-occultation	$\phi_{\rm mid-occultation}$	0.4998 ±0.0005
Occultation duration	T_{58} (d)	0.097 ±0.002
Duration of occultation ingress ≈ duration of occultation egress	$T_{56} \approx T_{78}$ (d)	0.024±0.002
Star mass	$M_\star$ ($M_\odot$)	1.10±0.03
Star radius	$R_\star$ ($R_\odot$)	1.29±0.05
Star surface gravity	$\log g_\star$ (cgs)	4.26 ±0.03
Star density	$\rho_\star$ ($\rho_\odot$)	0.52±0.06
Star effective temperature	$T_{\rm eff}$ (K)	6000±100
Star metallicity	[Fe/H]	−0.02±0.09
Planet mass	M_P ($M_{\rm Jup}$)	1.03±0.02
Planet radius	R_P ($R_{\rm Jup}$)	1.27 ±0.07
Planet surface gravity	$\log g_P$ (cgs)	3.16 ±0.04
Planet density	ρ_P (ρ_J)	0.50 ±0.08
Semi-major axis	a (au)	0.0398 ±0.0003
Occultation depth at 3.6 μm	$\Delta F_{3.6}$	0.001 26 ± 0.000 13
Occultation depth at 4.5 μm	$\Delta F_{4.5}$	0.001 49 ± 0.000 16
Planet equilibrium temperature (full redistribution)[a]	$T_{P,A=0,f=1}$ (K)	1623 ±43
Planet equilibrium temperature (day-side redistribution)[a]	$T_{P,A=0,f=2}$ (K)	1930 ± 51
Planet equilibrium temperature (instant reradiation)[a]	$T_{P,A=0,f=\frac{8}{3}}$ (K)	2074 ± 55

[a] A is the albedo, $f = 1$ is defined as full redistribution, $f = 2$ is day-side redistribution and $f = \frac{8}{3}$ is instant reradiation as in Smith et al. (2011).

wavelengths from the irradiated hemisphere of WASP-26b is consistent with the spectrum of an isothermal atmosphere, with the possibility of a weak thermal inversion within the uncertainties on the brightness temperatures.

5.2 Atmospheric analysis

We model the day-side emergent spectrum of the hot Jupiter WASP-26b using the atmospheric modelling and retrieval technique of Madhusudhan & Seager (2009, 2010). The model computes line-by-line radiative transfer in a plane-parallel atmosphere in local thermodynamic equilibrium, and assumes hydrostatic equilibrium and global energy balance. The pressure–temperature ($P-T$) profile of the atmosphere and the chemical composition, i.e. the sources of molecular line opacity, are input parameters to the model. The model atmosphere includes the major sources of opacity expected in hot, hydrogen-dominated atmospheres, namely molecular absorption due to H_2O, CO, CH_4 and CO_2, and continuum opacity due to H_2–H_2 collision-induced absorption. Our molecular line lists are discussed in Madhusudhan & Seager (2009) and Smith et al. (2012). Given a photometric or spectral data set of thermal emission from the planet, we explore the space of atmospheric chemical composition and temperature structure to determine the regions in model space that explain, or are excluded by, the data (e.g. Madhusudhan et al. 2011). In the present case, however, the number of available data points ($N = 2$) is far below the number of model parameters ($N = 10$), implying that a unique model fit to the data is not feasible. Consequently, we nominally fixed the chemical composition of the models to that obtained with solar elemental abundances in thermochemical equilibrium (e.g. Burrows & Sharp 1999; Madhusudhan 2012) for a given thermal profile, and explored the space of thermal profiles, with and without thermal inversions, that might explain the data.

Fig. 7 shows the 3.6 and 4.5 μm data along with the model spectra of atmospheres with and without a thermal inversion, and a blackbody model. All three models shown allow for very efficient day–night redistribution. We find that both our planet–star flux ratios can be explained by a planetary blackbody at around 1750 K. Consequently, the data are consistent with an isothermal atmosphere. However, an isothermal temperature profile may be unphysical in radiatively efficient atmospheres at low optical depth (e.g. Hansen 2008). A temperature profile with a non-zero thermal gradient, with or without a thermal inversion, may be more plausible. As shown in Fig. 7, the two data are fitted almost equally well by models with and without a thermal inversion, as shown by the red and green models, respectively. Further occultation depths measured at different wavelengths are required to break the degeneracies between the models and to determine the true nature of the atmosphere. It can be seen in Fig. 7 that there are some differences between the models with and without a thermal inversion at 1.25 (J band), 1.65 (H band) and 2.2 μm (K band). These wavelengths are accessible from the ground, so with measurements of the occultation depth at these wavelengths it may be possible to break the degeneracies between these models. *Hubble Space Telescope* WFC3 observations covering the wavelength range 1–1.7 μm can also be used to detect spectral features due to water either in emission or in absorption, and so distinguish between models with and without a thermal inversion (Madhusudhan 2012; Swain et al. 2012). We emphasize that we have only presented two possible models here that represent the average properties of the irradiated hemisphere of WASP-26b. With additional data other parameters of the models such as composition can be explored.

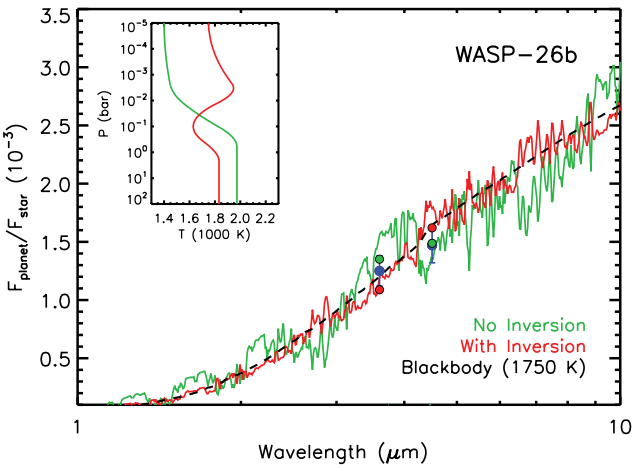

Figure 7. SED of WASP-26b relative to that of its host star. The blue circles with error bars denote our best-fitting occultation depths. The green line shows a model-atmosphere spectrum, based on a model which assumes solar abundances in thermochemical equilibrium and lacks a temperature inversion, and the dark red line shows a model with a temperature inversion. The band-integrated model fluxes are indicated with circles of the corresponding colours. The dashed black line shows a planetary blackbody model with a temperature of 1750 K. Inset: temperature–pressure profiles for our models.

5.3 Activity–inversion relation

Knutson, Howard & Isaacson (2010, hereafter K10) presented results which suggest that planets without thermal inversions orbit active stars, and those with inversions orbit inactive stars. This may be due to photodissociation of the opacity source in the upper atmosphere of the planet by the UV flux from the active stars (K10). It is known that solar-like stars have activity cycles on time-scales of approximately 10 yr. The Duncan et al. (1991) catalogue of S_{HK} activity measurements taken at the Mount Wilson Observatory was used to examine to what extent the activity of a star changes on short time-scales (of the order of months) and long time-scales (of the order of years). The aim was to determine if the variability in activity of the stars in the K10 sample was such that, in the time between the occultation observation and the measurement of $\log R'_{HK}$, the activity of the star can change enough to affect the interpretation of this activity–inversion relation. Recently, Montalto et al. (2012) showed that the activity of WASP-3 changed from $\log R'_{HK} = -4.95$ (less active) to -4.8 (more active) between 2007 and 2010. It has been shown by Menou & Rauscher (2009) that the time-scale for models of hot Jupiter atmospheres to go from their initial conditions to a statistical steady state was ~ 20 d. This suggests that the time-scale of hot Jupiter atmosphere variability is much shorter than the time-scale of stellar activity variability. More detailed modelling and additional observations are required to better understand whether variations in the UV irradiation can produce observable changes in the eclipse depths for planets near the boundary between atmospheres with and without strong thermal inversions.

We converted the S_{HK} measurements in Duncan et al. (1991) to $\log R'_{HK}$ using the method described by Noyes et al. (1984). A look-up table based on $\log R'_{HK}$ and $B - V$ colour for the stars in the Duncan et al. (1991) catalogue was then constructed. Using this table, the within-season variation of $\log R'_{HK}$ of the stars was used as a measure of the short-term variability in $\log R'_{HK}$ and the

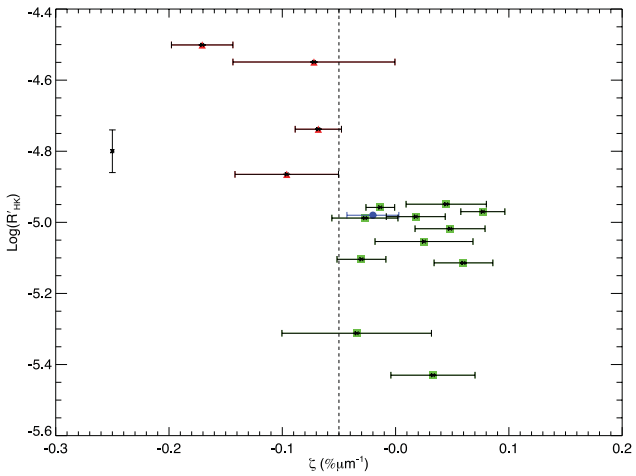

Figure 8. Activity–inversion plot for the stars in K10. Points on the left of the dotted line (triangles) denote non-inverted planets around active stars and those on the right of the dotted line (squares) denote inverted planets around inactive stars. The point on the left-hand side of the plot shows the typical change in log R'_{HK} (season to season), assuming measurements over several nights. The blue circle corresponds to WASP-26. The stars are listed in Table 5.

season-to-season variation in log R'_{HK} as a measure of the long-term variation in log R'_{HK}. This look-up table was then used to estimate the variation in log R'_{HK} for the stars of K10 based on their $B - V$ colour. It was found that the short-term variability was always $\leq$0.02 dex and the long-term variability was between 0.02 and 0.06 dex. This suggests that the variation in log R'_{HK} is not large enough on either short- or long-term time-scales to change the interpretation of K10. However, this may blur the boundary between the two classes of planets. The error bar shown in Fig. 8 shows the typical change in activity, assuming that the spectra are measured over several nights. It is possible for stars to vary by much more than this amount over their rotation period (e.g. Dumusque et al. 2012). This short time-scale variation will move the star on the diagram but this may not reflect changes in UV irradiation. The value of log $R'_{HK} = -4.98$ for WASP-26 used in this analysis is taken from Anderson et al. (2011b).

We compiled updated values of R_P/R_* and the secondary eclipse depths for the stars in the K10 sample (Table 5). Fig. 5 of K10 was then replotted; this is shown in Fig. 8. We include in this plot WASP-26b. As can be seen from Fig. 8, it seems to lie very close to the boundary between the two classes. Using the convention as in Anderson et al. (2011c) the abscissa value for WASP-26b is $\zeta = -0.020 \pm -0.023$ per cent μm^{-1}, where ζ is the gradient of the measurements at 3.6 and 4.5 μm, i.e. $\Delta F_{3.6} - \Delta F_{4.5}/(-0.9\mu m)$, minus the gradient of the blackbody that is the best fit to the two measurements. The theory behind this is that at 4.5 μm there are opacity sources that are not present at 3.6 μm (CO and H_2O) (Madhusudhan & Seager 2010). The 4.5 μm data probe a higher region of the atmosphere compared to the 3.6 μm data. This suggest that if the brightness temperature at 4.5 μm is greater than that at 3.6 μm, then there is likely to be a thermal inversion in the atmosphere.

5.4 Eccentrictiy

From secondary eclipse measurements, it is also possible to constrain the eccentricity of the orbit from timing of the secondary eclipse relative to transit. We find that the eccentricity of the orbit is small ($e = 0.0028^{+0.0097}_{-0.0022}$), which is consistent with a circular orbit at the 1σ level. We find a 3σ upper limit on the eccentricity of the planet's orbit of 0.0399 which is similar to Anderson et al. (2011b) 3σ upper limit of 0.048.

6 CONCLUSION

In this paper, we present new warm *Spitzer* photometry of WASP-26 at 3.6 and 4.5 μm along with new transit photometry taken in the *g*, *r* and *i* bands. We report the first detection of the occultation of WASP-26b with eclipse depths at 3.6 and 4.5 μm of 0.001 26 ± 0.000 13 and 0.001 49 ± 0.000 16, respectively, which correspond to brightness temperatures of 1825 ± 80 and 1725 ± 89 K. Our analysis shows that the atmosphere of WASP-26b is consistent with an isothermal atmosphere with the possibility of a weak thermal inversion (within the uncertainties on the brightness temperatures). If the K10 activity–inversion relation holds for WASP-26b, then we

Table 5. Stars in Fig. 8.

Star	Log(R'_{HK})	ζ value	R_P/R_*	Eclipse depth in channel 1	Eclipse depth in channel 2
HD 189733	−4.501[a]	−0.1707 ± 0.0271	Carter & Winn (2010)	Charbonneau et al. (2008)	Charbonneau et al. (2008)
TRES-3	−4.549[a]	−0.0721 ± 0.0715	Southworth (2011)	Fressin et al. (2010)	Fressin et al. (2010)
TRES-1	−4.738[a]	−0.0682 ± 0.0204	Southworth (2008)	Knutson et al. (2010)	Charbonneau et al. (2005)
WASP-4	−4.865[a]	−0.0961 ± 0.0457	Southworth et al. (2009b)	Beerer et al. (2011)	Beerer et al. (2011)
XO-2	−4.988[a]	−0.0271 ± 0.0292	Southworth (2010)	Machalek et al. (2009)	Machalek et al. (2009)
TRES-2	−4.949[a]	0.0447 ± 0.0354	Southworth (2011)	O'Donovan et al. (2010)	O'Donovan et al. (2010)
XO-1	−4.958[a]	−0.0135 ± 0.0127	Burke et al. (2010)	Machalek et al. (2008)	Machalek et al. (2008)
HAT-P-1	−4.984[a]	0.0178 ± 0.0260	Southworth (2008)	Todorov et al. (2010)	Todorov et al. (2010)
HD 209458	−4.970[a]	0.0770 ± 0.0194	Southworth (2008)	Knutson et al. (2008)	Knutson et al. (2008)
TRES-4	−5.104[a]	−0.0301 ± 0.0216	Southworth (2012)	Knutson et al. (2009)	Knutson et al. (2009)
COROT-1	−5.312[a]	−0.0343 ± 0.0660	Southworth (2011)	Deming et al. (2011)	Deming et al. (2011)
WASP-1	−5.114[a]	0.0599 ± 0.0259	Southworth (2008)	Wheatley et al. (2010)	Wheatley et al. (2010)
WASP-2	−5.054[a]	0.0251 ± 0.0432	Southworth et al. (2010)	Wheatley et al. (2010)	Wheatley et al. (2010)
WASP-18	−5.430[a]	0.0332 ± 0.0176	Southworth et al. (2009c)	Maxted et al. (2013)	Maxted et al. (2013)
HAT-P-7	−5.018[a]	0.0481 ± 0.0309	Southworth (2011)	Christiansen et al. (2010)	Christiansen et al. (2010)
WASP-26	−4.98[b]	−0.0200 ± 0.0229	This paper	This paper	This paper

[a]Log(R'_{HK}) value from Knutson et al. (2010).
[b]Log(R'_{HK}) value from Anderson et al. (2011b).

would expect it to host a thermal inversion. More secondary eclipse data at different wavelengths, particularly near-IR secondary eclipse depths near the peak of the planet's SED, will be able to better constrain the true nature of the atmosphere of WASP-26b.

ACKNOWLEDGEMENTS

DPM and JTR acknowledge the financial support from the Science and Technology Facilities Council (STFC) in the form of PhD studentships. JS acknowledges financial support from STFC in the form of an Advanced Fellowship. This work is based in part on observations made with the *Spitzer Space Telescope*, which is operated by the Jet Propulsion Laboratory, California Institute of Technology, under a contract with NASA. Support for this work was provided in part by NASA through awards issued by JPL/Caltech and by the Planetary Atmospheres Program, grant NNX12AI69G. NM acknowledges support from the Yale Center for Astronomy and Astrophysics (YCAA) at Yale University through the YCAA prize postdoctoral fellowship.

REFERENCES

Albrecht S. et al., 2012, ApJ, 757, 18
Anderson D. R. et al., 2011a, MNRAS, 416, 2108
Anderson D. R. et al., 2011b, A&A, 534, A16
Anderson D. R. et al., 2011c, preprint (arXiv:1112.5145)
Beerer I. M. et al., 2011, ApJ, 727, 23
Burke C. J. et al., 2010, ApJ, 719, 1796
Burrows A., Sharp C. M., 1999, ApJ, 512, 843
Carter J. A., Winn J. N., 2010, ApJ, 709, 1219
Charbonneau D. et al., 2005, ApJ, 626, 523
Charbonneau D., Knutson H. A., Barman T., Allen L. E., Mayor M., Megeath S. T., Queloz D., Udry S., 2008, ApJ, 686, 1341
Christiansen J. L. et al., 2010, ApJ, 710, 97
Claret A., 2004, A&A, 428, 1001
Collier Cameron A. et al., 2007, MNRAS, 380, 1230
Deming D., Seager S., Richardson L. J., Harrington J., 2005, Nat, 434, 740
Deming D. et al., 2011, ApJ, 726, 95
Dumusque X. et al., 2012, Nat, 491, 207
Duncan D. K. et al., 1991, ApJS, 76, 383
Eastman J., Siverd R., Gaudi B. S., 2010, PASP, 122, 935
Enoch B., Collier Cameron A., Parley N. R., Hebb L., 2010, A&A, 516, A33
Fazio G. G. et al., 2004, ApJS, 154, 10
Ford E. B., 2006, ApJ, 642, 505
Fortney J. J., Lodders K., Marley M. S., Freedman R. S., 2008, ApJ, 678, 1419
Fressin F., Knutson H. A., Charbonneau D., O'Donovan F. T., Burrows A., Deming D., Mandushev G., Spiegel D., 2010, ApJ, 711, 374
Gelman A., Carlin J. B., Stern H. S., Rubin D. B., 2003, Bayesian Data Analysis. Chapman and Hall, New York
Hansen B. M. S., 2008, ApJS, 179, 484
Knutson H. A., Charbonneau D., Allen L. E., Burrows A., Megeath S. T., 2008, ApJ, 673, 526
Knutson H. A., Charbonneau D., Burrows A., O'Donovan F. T., Mandushev G., 2009, ApJ, 691, 866
Knutson H. A., Howard A. W., Isaacson H., 2010, ApJ, 720, 1569 (K10)
Kurucz R. L., 1991, in Philip A. G. D., Upgren A. R., Janes K. A., eds, Precision Photometry: Astrophysics of the Galaxy. L. Davis Press, Schenectady, New York
Machalek P., McCullough P. R., Burke C. J., Valenti J. A., Burrows A., Hora J. L., 2008, ApJ, 684, 1427
Machalek P., McCullough P. R., Burrows A., Burke C. J., Hora J. L., Johns-Krull C. M., 2009, ApJ, 701, 514
Madhusudhan N., 2012, ApJ, 758, 36
Madhusudhan N., Seager S., 2009, ApJ, 707, 24
Madhusudhan N., Seager S., 2010, ApJ, 725, 261
Madhusudhan N. et al., 2011, Nat, 469, 64
Mandel K., Agol E., 2002, ApJ, 580, L171
Maxted P. F. L. et al., 2013, MNRAS, 428, 2645
Menou K., Rauscher E., 2009, ApJ, 700, 887
Montalto M. et al., 2012, MNRAS, 427, 2757
Noyes R. W., Hartmann L. W., Baliunas S. L., Duncan D. K., Vaughan A. H., 1984, ApJ, 279, 763
O'Donovan F. T., Charbonneau D., Harrington J., Madhusudhan N., Seager S., Deming D., Knutson H. A., 2010, ApJ, 710, 1551
Pollacco D. L. et al., 2006, PASP, 118, 1407
Pollacco D. et al., 2008, MNRAS, 385, 1576
Schwarz G., 1978, Ann. Stat., 6, 461
Seager S., Mallén-Ornelas G., 2003, ApJ, 585, 1038
Smalley B. et al., 2010, A&A, 520, A56
Smith A. M. S., Anderson D. R., Skillen I., Collier Cameron A., Smalley B., 2011, MNRAS, 416, 2096
Smith A. M. S. et al., 2012, A&A, 545, A93
Southworth J., 2008, MNRAS, 386, 1644
Southworth J., 2010, MNRAS, 408, 1689
Southworth J., 2011, MNRAS, 417, 2166
Southworth J., 2012, MNRAS, 426, 1291
Southworth J. et al., 2009a, MNRAS, 396, 1023
Southworth J. et al., 2009b, MNRAS, 399, 287
Southworth J. et al., 2009c, ApJ, 707, 167
Southworth J. et al., 2010, MNRAS, 408, 1680
Southworth J., Mancini L., Maxted P. F. L., Bruni I., Tregloan-Reed J., Barbieri M., Ruocco N., Wheatley P. J., 2012, MNRAS, 422, 3099
Spiegel D. S., Silverio K., Burrows A., 2009, ApJ, 699, 1487
Stetson P. B., 1987, PASP, 99, 191
Swain M. et al., 2012, preprint (arXiv:1205.4736)
Todorov K., Deming D., Harrington J., Stevenson K. B., Bowman W. C., Nymeyer S., Fortney J. J., Bakos G. A., 2010, ApJ, 708, 498
Todorov K. O. et al., 2012, ApJ, 746, A111
Werner M. W. et al., 2004, ApJS, 154, 1
Wheatley P. J. et al., 2010, preprint (arXiv:1004.0836)
Zahnle K., Marley M., Freedman R., Lodders K., Fortney J., 2009, ApJ, 701

This paper has been typeset from a TEX/LATEX file prepared by the author.